Available online at www.sciencedirect.com
SCIENCE DIRECT
Journal of Magnetic Resonance 181 (2006) 135–147
JMR Journal of Magnetic Resonance
www.elsevier.com/locate/jmr

$T_{1\rho}$ MRI contrast in the human brain: Modulation of the longitudinal rotating frame relaxation shutter-speed during an adiabatic RF pulse

Shalom Michaeli [a,*], Dennis J. Sorce [a], Charles S. Springer Jr. [b], Kamil Ugurbil [a], Michael Garwood [a]

[a] Center for Magnetic Resonance Research, Department of Radiology, University of Minnesota Medical School, Minneapolis, MN 55455, USA
[b] Advanced Imaging Research Center, Oregon Health and Science University, Portland, OR, USA

Received 9 November 2005; revised 6 March 2006
Available online 3 May 2006

Abstract

Longitudinal relaxation in the rotating frame ($T_{1\rho}$) is the dominant mechanism during a train of adiabatic full passage (AFP) RF pulses with no interpulse intervals, placed prior to an excitation pulse. Asymptotic apparent time constants ($T'_{1\rho}$) were measured for human occipital lobe ^1H_2O at 4 T using brief imaging readouts following such pulse trains. Two members of the hyperbolic secant (HSn) AFP pulse family ($n = 1$ or 4; i.e., arising from different amplitude- and frequency-modulation functions) were used. These produced two different non-monoexponential signal decays during the pulse trains. Thus, there are differing contrasts in asymptotic $T'_{1\rho}$ maps derived from these data. This behavior is quite different than that of ^1H_2O signals from an aqueous protein solution of roughly the same macromolecular volume fraction as tissue. The ROI-averaged decays from the two acquisitions can be simultaneously accommodated by a two-site-exchange model for an equilibrium isochronous process whose exchange condition is modulated during the pulse. The model employs a two-spin description of dipolar interaction fluctuations in each site. The intrinsic site $R_{1\rho}$ ($\equiv T_{1\rho}^{-1}$) value is sensitive to fluctuations at the effective Larmor frequency (ω_{eff}) in the rotating frame, and this is modulated differently during the two types of AFP pulses. Agreement with the data is quite good for site orientation correlation time constants characteristic of macromolecule-interacting water (site A) and bulk-like water (site B). Since $R_{1\rho A}$ is significantly modulated while $R_{1\rho B}$ is not, the intrinsic relaxographic shutter-speed for the process ($\equiv |R_{1\rho A} - R_{1\rho B}|$), and thus the exchange condition, is modulated. However, the mean residence time (67 ms) and intrinsic population fraction (0.2) values found for site A are each rather larger than might be expected, suggesting a disproportionate role for the water molecules known to be "buried" within the large and concentrated macromolecules of in vivo tissue.

Keywords: $T_{1\rho}$ contrast; Adiabatic pulses; Shutter-speed; Dipolar relaxation

1. Introduction

Conventionally, MRI contrast is generated by the tissue variation of free-precession longitudinal (time constant, T_1) and/or transverse (time constant, T_2) relaxation of the ^1H_2O MR signal. The orientational references of these are relative to the laboratory frame, in which the direction of the main magnetic field defines the longitudinal axis, Z. However, there have been several recent investigations of spatially encoded in vivo ^1H_2O relaxation occurring in the presence of radio frequency (RF) irradiation, referred to as rotating frame relaxation. The relaxation of magnetization parallel to the longitudinal axis (Z') of that reference frame is characterized with the time constant $T_{1\rho}$, while that of magnetization in the plane perpendicular to Z' with the time constant $T_{2\rho}$. These reports have shown $T_{1\rho}$-related contrast in, for example, rat cerebral ischemia [1] and human knee cartilage [2] and $T_{2\rho}$-related contrast in the human brain [3,4].

* Corresponding author. Fax: +1 612 626 2004.
E-mail address: shalom@cmrr.umn.edu (S. Michaeli).

1090-7807/$ - see front matter © 2006 Elsevier Inc. All rights reserved.
doi:10.1016/j.jmr.2006.04.002

The in vivo $T_{1\rho}$ studies reported to date have employed pulse sequences utilizing a traditional "continuous wave" (CW) RF "spin lock," that is, with a constant irradiation frequency (ω_{RF}). Here, we report the first in vivo ^1H_2O $T_{1\rho}$ images (of the human occipital cortex) obtained when the spin lock is accomplished with a train of contiguous, so-called "adiabatic" (frequency-swept) modulated RF pulses. Moreover, we have used two different RF modulation functions to effect the adiabatic pulses. (After this manuscript was submitted, a report appeared on simulations of the use of modulated adiabatic waveforms to accomplish the spin lock [5].)

The rate constant for laboratory frame longitudinal relaxation (R_1) is particularly sensitive to the molecular fluctuations of magnetic dipolar interactions, but only those at high frequencies near that (ω_0) of the Larmor precession (i.e., in the MHz range) [6]. There is good reason to believe that the most effective dipolar fluctuations in tissue occur at much lower frequencies (i.e., in the kHz range) [6]. It has long been understood that the rotating frame longitudinal relaxation rate constant ($R_{1\rho}$) is driven principally by dipolar fluctuations at frequencies near that (ω_{eff}) in the simultaneous presence of the RF and laboratory magnetic fields (the *effective* precession frequency). Since this can be "tuned" by adjustment of ω_1, the (Rabi) frequency measure of the RF *amplitude*, it has been anticipated that this can provide experimental access to the relevant lower frequencies. However, an NMR measurement of the kinetics of a process (say, an equilibrium molecular exchange) can be accomplished only if the kinetics can be varied relative to the inherent "shutter-speed" of the NMR experiment, or vice versa [7]. Since in vivo studies are constrained to an isothermal condition (37 °C), process kinetics cannot be altered. Thus, the shutter-speed must be varied. With the traditional CW spin lock, this can be accomplished only with time-consuming incrementation of ω_1 [8], or of the "off-resonance" frequency difference $|\omega_{RF} - \omega_0|$ [9]. However, an important property of the adiabatic pulse is that the magnitude of ω_{eff} is inherently modulated *during* its time-course. We have taken advantage of this feature.

For the interpretation of NMR data, dynamic processes can often be modeled with a parsimonious equilibrium two-site-exchange (2SX) system approximation. Thus, we have applied the theoretical formalisms for simultaneous rotating frame dipolar relaxation and 2SX equilibrium maintained during the adiabatic pulse. We find that we can successfully account for our experimental results with fundamental parameters for tissue water dynamics that are not unreasonable.

2. Theory

2.1. Adiabatic pulse effects on $T_{1\rho}$ relaxation concurrent with equilibrium exchange between two sites

During the courses of adiabatic full-passage (AFP) pulses, the decay of magnetization aligned along the *time-dependent* effective magnetic field direction $\boldsymbol{\omega}_{\mathbf{eff}}(\boldsymbol{t})$ is referred to as longitudinal relaxation in the rotating frame, characterized by $T_{1\rho}(t)$. During an adiabatic pulse, both the orientation (measured by the angle α) and the magnitude of ω_{eff} in the frequency-modulated rotating frame vary continuously [10,11]. In the 2SX model, there are two magnetization populations contributing to the signal intensity (SI). Even without resonance frequency differences between the exchanging spins, $\delta\omega = 0$ (the isochronous case), the SI time-course can be biexponential when the exchange system is in the intermediate or slow exchange conditions [12,13]. Thus, during our pulse sequence (Fig. 1a), which includes an AFP pulse train of length TL ($= mT_p$, where m is the number of AFP pulses and T_p is the duration of each pulse), the SI time-course can be written as:

$$\begin{aligned}\frac{SI(t)}{SI_0} = {} & \frac{1}{T_p}\int_0^{T_p} P'_A(t)\,dt \exp\left\{-m\int_0^{T_p} R'_{1\rho A}(t)\,dt\right. \\ & -\left\langle R'_{1\rho(A)AHP}\right\rangle T_{AHP} - 2\left\langle R'_{2\rho(A)AFP}\right\rangle T_{AFP} \\ & \left. -R_{2A}(TE - 2T_p)\right\} \\ & + \frac{1}{T_p}\int_0^{T_p} P'_B(t)\,dt \exp\left\{-m\int_0^{T_p} R'_{1\rho B}(t)\,dt\right. \\ & -\left\langle R'_{1\rho(B)AHP}\right\rangle T_{AHP} - 2\left\langle R'_{2\rho(B)AFP}\right\rangle T_{AFP} \\ & \left. -R_{2B}(TE - 2T_p)\right\}, \end{aligned} \tag{1}$$

where

$$\left\langle R'_{1\rho(A,B)AHP}\right\rangle = \frac{1}{T_{AHP}}\int_{TL}^{TL+T_{AHP}} R'_{1\rho(A,B)AHP}(t)\,dt \tag{1a}$$

and

$$\left\langle R'_{2\rho(A,B)AFP}\right\rangle = \frac{1}{T_p}\int_{TL+T_{AHP}}^{TL+T_{AHP}+T_p} R'_{2\rho(A,B)AFP}(t)\,dt. \tag{1b}$$

Here, $P'_A(t), P'_B(t), R'_{1\rho A}(t)$, and $R'_{1\rho B}(t)$ are the *apparent* populations and relaxation rate constants of the A and B magnetization pools (as affected by the exchange), and SI_0 is the signal intensity when $t = 0$. The total time for the SI decay during the Fig. 1a pulse sequence includes the periods of: (a) the AFP pulse train of length TL, (b) the adiabatic half passage (AHP) excitation pulse of duration T_{AHP}, and (c) the slice selection time period TE. Thus, $TD = TL + T_{AHP} + TE$. Eq. (1) states that relaxation is governed solely by $T_{1\rho}$ during TL, governed by $T_{1\rho}$ during the AHP, and by $T_{2\rho}$ during the two slice selecting AFP pulses ([3,10,11]) and relaxation is governed by free precession T_2 relaxation during the time interval $(TE - 2T_p)$. The $(T_{AHP} + TE)$ period is constant for all acquisitions, and will be dealt with here by extrapolation. We will see that the apparent relaxation rate constants and populations are time dependent during the RF irradiation.

The theory of $T_{1\rho}$ relaxation in the presence of equilibrium anisochronous exchange, e.g., between spins with different resonance frequencies, $\delta\omega \neq 0$, is well established [14–16]. Here, we consider the effect of an isochronous

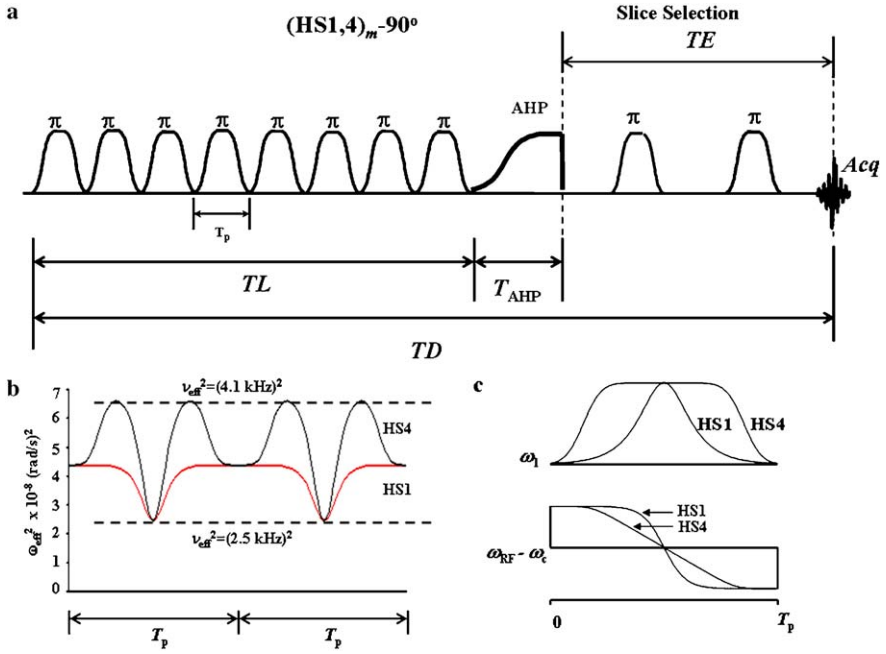

Fig. 1. (a) The fully adiabatic $(HS1)_m$-90° or $(HS4)_m$-90° RF pulse timing diagram is presented. The slice selection and the spiral readout gradient pulses are not shown. The total SI decay time is TD = TL + T_{AHP} + TE, where the AFP pulse train duration is TL, the excitation AHP pulse duration is T_{AHP}, and the constant slice selection segment is denoted by TE. (b) The ν_{eff}^2 time courses during two contiguous HS1 and HS4 pulses are plotted. The dashed lines represent highest and lowest values of ν_{eff}^2 during the HS4 pulse. (c) Amplitude (top) and frequency (bottom) modulation functions in the FM frame for two different AFP pulses, HS1 and HS4 [9].

exchange ($\delta\omega = 0$, out between spins at sites A and B having different relaxation rate constants in the absence of exchange) maintaining equilibrium during the RF irradiation. The well-known equations describing the instantaneous apparent relaxation rate constants and populations of the sites A and B undergoing 2SX can be written for the time-dependent $T_{1\rho}(t)$ as [12,13,17]:

$$R'_{1\rho A}(t) = \tfrac{1}{2}\Big\{R_{1\rho A}(t) + R_{1\rho B}(t) + k_A + k_B + \Big[(R_{1\rho A}(t) - R_{1\rho B}(t) + k_A - k_B)^2 + 4k_A k_B\Big]^{1/2}\Big\}, \tag{2}$$

$$R'_{1\rho B}(t) = \tfrac{1}{2}\Big\{R_{1\rho A}(t) + R_{1\rho B}(t) + k_A + k_B - \Big[(R_{1\rho A}(t) - R_{1\rho B}(t) + k_A - k_B)^2 + 4k_A k_B\Big]^{1/2}\Big\}, \tag{3}$$

$$P'_B(t) = \frac{1}{(R'_{1\rho B}(t) - R'_{1\rho A}(t))}(P_A R_{1\rho A}(t) + P_B R_{1\rho B}(t) - R'_{1\rho A}(t)) : P'_A(t) = 1 - P'_B(t). \tag{4}$$

Here, $R_{1\rho A}(t)$ and $R_{1\rho B}(t)$ are the *intrinsic* longitudinal rotating-frame relaxation rate constants of sites A and B magnetizations in the absence of exchange, P_A and P_B are the *intrinsic* equilibrium populations (mole fractions) of spins in magnetic sites A and B, respectively, and k_A and k_B are the unidirectional rate constants for site egress (i.e., τ_A^{-1} and τ_B^{-1}, respectively). The relaxation rate constants $R_{1\rho A,B}(t)$ represent relaxation from mechanisms other than the equilibrium exchange, such as dipolar interactions, cross-relaxations, and cross-correlations. Thus, the *fixed* physiological parameters of an isothermal tissue system are P_A, k_A, P_B, and k_B. These are not independent of each other: the McConnell relationship is $P_A\, k_A = P_B\, k_B$ [18]. The measure of equilibrium kinetics is the rate constant: $k = k_A + k_B$. Eqs. (2)–(4) suggest that, in the presence of isochronous 2SX, the apparent rotating frame relaxation rate constant and population of the site A ($R'_{1\rho A}(t)$ and $P'_A(t)$, respectively) can depend on the intrinsic parameters of site B ($R_{1\rho,\,B}(t)$ and P_B), and vice versa.

In the fast-exchange-limit (FXL), the relaxation has a single-valued rate constant (even though it varies during the adiabatic rotation), $R'_{1\rho}$, given by Woessner and Zimmerman [12,13]:

$$R'_{1\rho}(t) = P_A R_{1\rho A}(t) + P_B R_{1\rho B}(t) \tag{5}$$

and can be identified with whichever of $R_{1\rho A}(t)$ and $R_{1\rho B}(t)$ is smaller [17]. At the other extreme, the slow-exchange-limit (SXL), $P'_A = P_A$ and $P'_B = P_B$, and we have: $R'_{1\rho A}(t) = R_{1\rho A}(t) + k_A$, and $R'_{1\rho B}(t) = R_{1\rho B}(t) + k_B$ [12,13].

Now, we will expand the intrinsic rotating frame relaxation rate constants ($R_{1\rho A}(t)$ and $R_{1\rho B}(t)$) for site A and B magnetizations in terms of dipole–dipole interactions between two identical spins in each site and their resulting auto-relaxations (cross-relaxations and cross-correlations are not explicitly considered here: they are implicit). The expressions for these interactions can be used to estimate

pulse time-course dependencies for $R_{1\rho A}(t)$ and $R_{1\rho B}(t)$ in Eqs. (2)–(4). The two sites might be thought of as, for example, macromolecule-interacting water (along with macromolecular protons with which water protons might exchange) and bulk-like water.

3. Relaxation in each site

3.1. The isolated two-spin description (A_2 or B_2)

For a system of two equivalent nuclei of spin I and gyromagnetic ratio γ in a single site, the instantaneous rotating frame longitudinal relaxation rate constant contribution from the dipolar fluctuations can be given by a simple, isolated two-spin description [19]:

$$R_{1\rho,\mathrm{dd}}(t) = \frac{1}{(10k_{\mathrm{dd}})}\left[\frac{3\sin^2\alpha(t)\cos^2\alpha(t)}{1+\omega_{\mathrm{eff}}^2(t)\tau_c^2} + \frac{3\sin^4\alpha(t)}{1+4\omega_{\mathrm{eff}}^2(t)\tau_c^2} + \frac{2+3\sin^2\alpha(t)}{1+\omega_0^2\tau_c^2} + \frac{8-6\sin^2\alpha(t)}{1+4\omega_0^2\tau_c^2}\right], \quad (6)$$

where $\frac{1}{k_{\mathrm{dd}}} = 2I(I+1)\hbar^2\gamma^4 r^{-6}\tau_c$, r is the internuclear distance, τ_c is the correlation time for tumbling of its vector, $\hbar$ is Dirac's constant, and t is the elapsed AFP pulse time. Similar to $R_{2\rho,\,\mathrm{dd}}$ relaxation [13], Eq. (6) can be used to calculate the time-courses of the two different site $R_{1\rho,\,\mathrm{dd}}$ values during the AFP pulses. In each of the sites, τ_c and r can (and at least τ_c generally will) be different, and therefore, τ_{cA}, τ_{cB}, r_A, and r_B are additional fundamental parameters characterizing the physiological system.

Now, $R_{1\rho}(t)$ ($\equiv R_{1\rho,\,\mathrm{dd}}(t)$) is time-dependent as a result of modulating the pulse functions, $\omega_1(t)$ and $\omega_{\mathrm{RF}}(t)$. (Here, $\omega_1(t)$ and $\omega_{\mathrm{RF}}(t)$ each have units of rad/s.) Detailed descriptions of the HSn adiabatic pulse modulation functions are given in [10,20]. Briefly, HSn pulses are stretched versions of the hyperbolic secant pulse [21], and n denotes the stretching factor. According to this description, the original hyperbolic secant pulse is referred to as the HS1 pulse. As n becomes larger, the HSn pulse amplitude-modulation (AM) function becomes flatter, and progressively resembles that of the chirp pulse (e.g., the AM function flattens and the frequency sweep approaches linearity) (Fig. 1c). Thus, the time evolution of magnetization during an HSn pulse can change significantly with a change of n.

During an AFP pulse, $\omega_{\mathrm{eff}}(t)$ changes its orientation in the laboratory frame at the instantaneous angular velocity, $\mathrm{d}\alpha(t)/\mathrm{d}t$, with:

$$\alpha(t) = \tan^{-1}\left(\frac{\omega_1(t)}{\Delta\omega(t)}\right), \quad (7)$$

where $\Delta\omega(t) = (\omega_0 - \omega_{\mathrm{RF}}(t))$. In classical analyses of adiabatic pulses, it is convenient to consider the vector components of the magnetic fields and magnetization (**M**) in a reference frame that rotates at the instantaneous RF pulse frequency, $\omega_{\mathrm{RF}}(t)$, and is known as the frequency-modulated (FM) frame. We note that the magnitude of the effective field frequency during an adiabatic pulse is also modulated, and is given by:

$$\omega_{\mathrm{eff}}(t) = \sqrt{\omega_1^2(t) + \Delta\omega^2(t)}. \quad (8)$$

The pulse time-dependencies of squares of this quantity are plotted in Fig. 1b for adjacent pairs of the HS1 and HS4 AFP pulses used here.

Eqs. (7) and (8) allow us to insert the effects of the pulse-producing modulation functions into Eq. (6) and this provides an explanation for the pulse duration time-course dependence. Because ω_{eff} varies, the magnetization responds to *varying* portions of the global motion spectrum (J) [6] during the pulse. It is important to note that there is an Eq. (6) for each site, A and B. These produce the $R_{1\rho A}(t)$ and $R_{1\rho B}(t)$ values for Eqs. (2)–(4), which, along with the P_A, P_B, k_A, and k_B values, ultimately give the $R'_{1\rho A}(t)$, $R'_{1\rho B}(t)$, $P'_A(t)$, and $P'_B(t)$ values for Eq. (1), which can in turn give the pulse train length dependence of the SI.

The condition of the exchange system, which can range from the FXL to the SXL, depends on the comparison of the relevant shutter-speed for the exchange process, τ^{-1} (Cyrillic t), with k (FXL: $\tau^{-1} \ll k$; SXL: $\tau^{-1} \gg k$) [17]. Here, the rotating frame, longitudinal relaxographic $\tau_{1\rho}^{-1} \equiv |R_{1\rho A}(t) - R_{1\rho B}(t)|$. Though k is invariant in isothermal tissue, $R_{1\rho A}$ and $R_{1\rho B}$ can be functions of t during the pulse (as we have seen). Since $R_{1\rho A}(t)$ almost certainly varies *differently* than $R_{1\rho B}(t)$, $\tau_{1\rho}^{-1}$ varies during the pulse. Thus, the exchange condition can vary during the course of the AFP pulse.

4. Methods

For phantom sample measurements, hen egg white lysozyme (Sigma L-6876, Grade I) was hydrated by adding 80% phosphate buffered saline by mass to solid protein [36,37], and thoroughly mixed by swirling. $T_{1\rho}$ measurements of ^1H_2O signals from this solution were performed with an MRI system having a Varian Unity INOVA console (Varian Associates, CA, USA) interfaced to a 40 cm (horizontal) bore 4.7 T magnet (OMT, Inc., Oxon, UK). The 15 mL sample was held in a cylindrical container with its axis parallel to the magnet Y-axis, and placed adjacent to a surface RF transceiver coil. The solution was studied at ambient temperature, and did not settle during the ~10 minute acquisition. A localized spectroscopy pulse sequence [10], with the train of adiabatic pulses placed prior to the localization portion, was employed.

Human experiments were performed according to procedures approved by the Institutional Review Board of the University of Minnesota Medical School. After obtaining informed consent, studies on healthy volunteers were conducted with an MRI system having a Varian Unity INOVA console (Varian Associates, CA, USA) interfaced to a 90 cm bore 4 T magnet (OMT, Inc., Oxon, UK). A ^1H quadrature surface RF transceiver coil assembly, consisting of two geometrically decoupled turns (each 7 cm

in diameter), was used for the measurements. Shimming was performed with a fully adiabatic version of FASTMAP (Fast Automatic Shimming Technique by Mapping Along Projections) [22]. Gradient-echo TurboFLASH images [23] were first acquired for all subjects to define the slice orientation and position in the human visual cortex for the adiabatic $T'_{1\rho}$ measurements.

The fat signal at 1.3 ppm was suppressed with variable-power RF pulses having optimized relaxation delays, VAPOR [24], placed prior to the AFP pulse train. Because $T'_{1\rho}$ relaxation depends on the pulse modulation functions of the adiabatic pulse train only, the slice selection and imaging readout portions of the pulse sequence create a constant weighting and thus do not affect the measured relaxation rates. Here we used the TurboFLASH or spiral imaging readouts. With the gradient-echo TurboFLASH imaging readout, four segments were used. With a segmented spiral readout [25], eight segments were used (acquisition time = 35 ms). $T'_{1\rho}$ images of the occipital cortex were measured using $(0.70\,\text{mm})^2$ in-plane resolution, FOV = $(18\,\text{cm})^2$, 256^2 matrix, and slice thickness = 3 mm. Thus, the digital pixel area is $0.49\,\text{mm}^2$ and voxel volume is 1.5 μL. Two pre-scans were executed in all experiments in order to achieve an MR steady-state prior to data collection.

Of course, the AFP pulse can be effected in more than one way. Our $T'_{1\rho}$ measurements were performed using variable numbers (m) of HS1 or HS4 pulses in the AFP train placed prior to coherence excitation with an AHP pulse. Here, slice selection was performed with the two HS1 pulses applied in the presence of slice selection gradients (Fig. 1) and spiral imaging readout was used. These sequences are denoted $(\text{HS1})_m$-90° and $(\text{HS4})_m$-90°. Every AFP pulse had a bandwidth of 6.6 kHz and T_p set to 3 ms. The optimum RF power levels were determined for both HS1 and HS4 pulses using the region-of-interest (ROI) signals. The RF amplitude was calibrated by using a 400 μs hard pulse and varying its amplitude until a 90° nutation was achieved. The calibration experiments showed that the RF power settings used for the HS1 and HS4 pulses produced amplitudes $(\omega_1^{\max}/2\pi)$ equal to ~2.5 kHz. Because imaging was localized to the same brain region in all experiments, the RF power required to achieve the adiabatic condition varied by only 1–2 dB between subjects. The overall AFP train length (TD) was incremented by increasing the number (m) of AFP pulses in multiples of four with relative phases set according to MLEV 4 [26]. Five images were collected with TL values of 12, 24, 36, 48, and 60 ms (m = 4, 8, 12, 16, and 20). The 4 ms AHP excitation pulse and the slice selection portion (TE = 10 ms) was the same in all measurements. Thus, the total time of the signal decay was TD = TL + 14 ms. Interleaved acquisitions with the HS1 and HS4 AFP pulse trains were accomplished in order to minimize miss-registrations of the image slices.

Specific absorption rate (SAR) values were computed with the conservative assumption that all RF energy was deposited into 1 kg of brain tissue. The RF energy deposited by the AFP pulse train increases with m, and was kept below the FDA limit for the longest AFP pulse train. The SAR values were below the FDA guidelines (http://www.fda.gov/cdrh/ode/mri340.pdf). Calculated SAR values were 2.43 W/kg with the maximum number of AFP pulses (m = 20). This calculation included the fat suppression (VAPOR) and slice selection portions of the pulse sequences. Computed SAR values were in good agreement with the hardware SAR monitor of the system. It should be noted that the power deposition during VAPOR is very small due to the low power used for this portion of the pulse sequences (~0.01 W/kg). $T_{1\rho}$ measurements of one brain slice with the HS1 and HS4 pulses required ~11 min (TR = 7 s), and the total scan time (including shimming. RF calibrations, scout imaging, and slice positioning) was less than one hour per subject.

Experimental results were analyzed as described below. Asymptotic $T'_{1\rho}$ maps from the human measurements were generated using the MATLAB software package (MATLAB 6.1, Mathworks, MA).

5. Results

The dependence of the ^1H_2O $R'_{1\rho}$ rate constants on the HS1 and HS4 AFP pulse modulation functions was investigated using the $(\text{HS1})_m$-90° and $(\text{HS4})_m$-90° pulse sequences. The length of the AFP pulse train was incremented, with no interpulse intervals. The 4.7 T phantom sample and 4 T averaged multisubject (n = 5) log (SI/SI$_0$) decay curves are shown in Fig. 2. Though the phantom data (upper plots) decay slowly and monoexponentially,

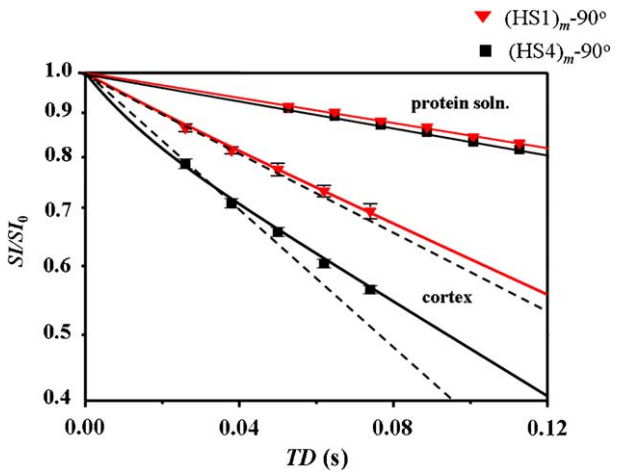

Fig. 2. The logarithm of the normalized SI is plotted as a function of TD. It is separately measured with the $(\text{HS1})_m$-90° (red triangles) and $(\text{HS4})_m$-90° (black squares) pulse sequences. The upper points report results for the lysozyme solution phantom sample, while the lower points and error bars report the mean (±SD) for coronal occipital cortex ROIs in five subjects. The dashed lines indicate the asymptotic behaviors of the SI decays, and would represent monoexponential relaxations. The superimposed red and black solid lines and curves are computer simulations of the SI decays using the equations and parameters listed in Table 1.

the human brain data (lower plots) do not. It is well documented that brain tissue ^1H_2O SI decay often exhibits non-monoexponentiality (for example, see [17] and references therein). The unavoidable slice selection interval of our acquisition (Fig. 1a) may cause us to miss early decay details. Because of the relatively small maximum TD values used in the human studies, we presume that the later portion of a multi exponential SI decay curve also almost certainly escaped complete acquisition. Indeed, SI has decayed at most only ~45% when our acquisition ends. However, the data exhibit clear differences with the $(HS1)_m$-90° (red triangles) and $(HS4)_m$-90° (black squares) pulse sequences. The human signals arose from ~2.7 mL coronal occipital cortex ROIs. (That for one subject is shown with a green border in the coronal T_1-weighted image in Fig. 3a.) The error bars represent the SEMs for the five subjects. The SI_0 values were estimated by extrapolating the first two points of log (SI) vs. TD plots (not shown) back to the left ordinate. Both cortex plots (lower) exhibit distinct curvature (compare with the dashed straight lines, tangent at the origin): thus, they each deviate from a single exponential function. However, it is clear that though the initial slope of the data from the HS1 acquisition has the smaller (less negative) value, the data from the HS4 acquisition show the greater departure from mono-exponentiality. The dashed lines correspond to asymptotic $R'_{1\rho}$ values of 5.65 s^{-1} and 9.23 s^{-1}, for the HS1 and HS4 decays, respectively. These, in turn, correspond to asymptotic $T'_{1\rho}$ values of 178 ms (HS1) and 108 ms (HS4).

Coronal asymptotic $T'_{1\rho}$ maps of the 2.7 mL ROI of the Fig. 3a subject were generated from the pixel-by-pixel $(HS1)_m$-90° (Fig. 3b) and $(HS4)_m$-90° (Fig. 3c) data. The $T'_{1\rho}$ values were estimated by fitting the initial portions of the individual pixel signal intensity decays to monoexponential functions (analogous to the Fig. 2 dashed straight lines). For the analysis, ~1600 pixels were used. Because no interpulse delays were used in the AFP train, the relaxation is dominated by $T_{1\rho}$ processes. The differences in the two $T'_{1\rho}$ maps indicate changes due to the different AFP pulse modulation functions used, and represent contrast generated almost exclusively by $T_{1\rho}$ relaxation. The asymptotic $T'_{1\rho}$ relaxation time constant differences are clearly seen in the Fig. 3d relaxograms, which were generated from the same ROI in the two maps. The greater breadth of the HS1 relaxographic peak supports the contention that the greater curvature of the HS4 decay in Fig. 2 is not due simply to ROI heterogeneity. Significant contrast is seen in each of the two asymptotic $T'_{1\rho}$ maps, which are displayed with the same color scale. As might be expected, sulcal spaces containing cerebrospinal fluid (CSF) exhibit larger $T'_{1\rho}$ values, making manifest the sensitivity of the adiabatic $T'_{1\rho}$ to a range of motional correlation times. Thus, the contrast is rather the opposite of that in the T_1-weighted image.

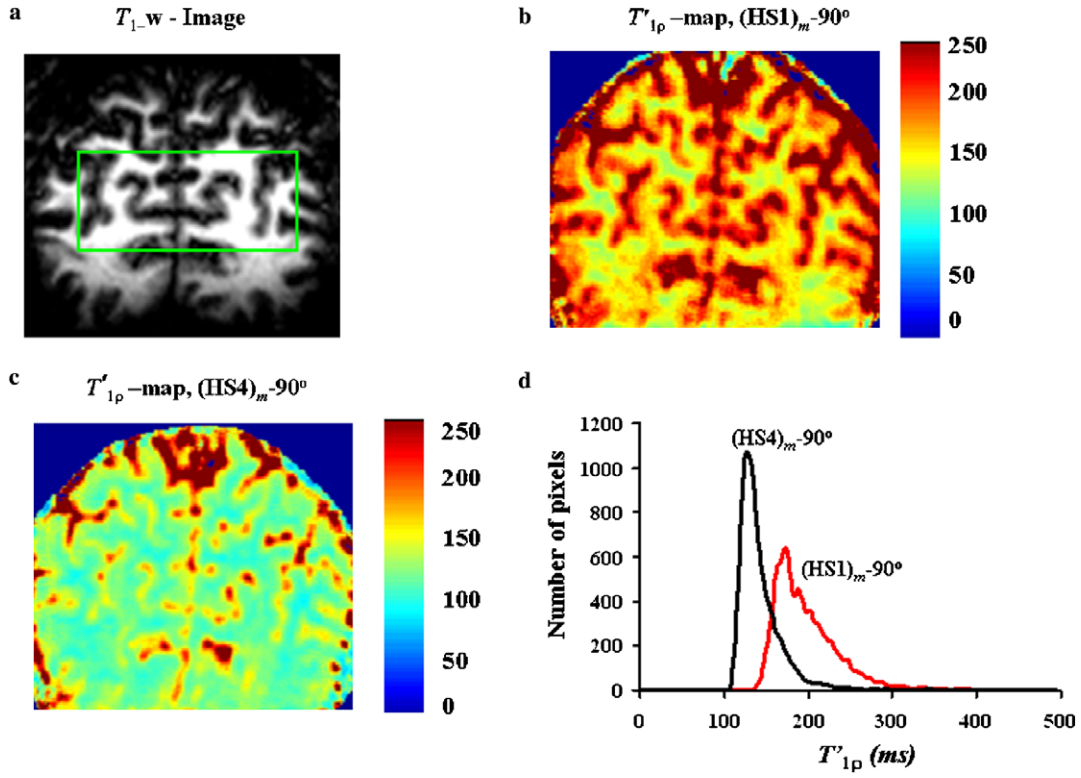

Fig. 3. (a) A T_1-weighted brain coronal image slice in the visual cortex V1 is shown for one subject (TR = 4 s). The green border circumscribes the ROI yielding the asymptotic $T'_{1\rho}$ maps measured with the (b) $(HS1)_m$-90°, and (c) $(HS4)_m$-90° pulse sequences using spiral imaging readout and displayed on the same color scale. (d) The asymptotic $T'_{1\rho}$ relaxograms from this ROI are plotted as red (HS1) and black (HS4) distributions. The averaged data for ROIs such as this are those plotted in Fig. 2.

6. Discussion

We now turn to molecular mechanistic interpretations of the in vivo adiabatic $T'_{1\rho}$ relaxation contrast detected. Brain water molecular interactions are characterized by different τ_c values corresponding to different water environments, such as the hydrated myelin sheet, the cytoplasm, or the CSF. The type of tissue ^1H_2O NMR relaxation measured here arises mainly from dipolar interactions modulated by complicated mechanisms that include equilibrium water exchange and magnetic interactions between the protons of different environments. In the interpretation of ^1H_2O $T_{1\rho}$ relaxation dispersion, there are at least three issues to be considered: (1) equilibrium water molecule exchange between different, averaged water populations; (2) orientational order of ^1H dipolar interactions within a population; (3) the effects of auto-relaxations, cross-relaxations and cross-correlations between different types of dipolar interactions (some chemical shift anisotropy could also be considered) within a population. Here, we focus on issue 1—the most significant—and use the most parsimonious model, comprising two water populations coupled by an equilibrium exchange (Eqs. (1)–(5)). To investigate issues 2 and 3, one could use the solution of the relaxation matrix [27]. In unpublished analyses, we have employed a three-spin description of each site to further explore these, and find that they can be subsumed within the τ_c value characterizing a population.

Recent laboratory frame relaxation (T_1) studies with compartmentalized contrast reagents (CRs) have shown that the 2SX model can be used to extract tissue compartmental water populations and the mean lifetimes of water molecules in them (τ_A and τ_B) from experimental data [28–32]. Here, we demonstrate that the differences in the adiabatic pulse modulation functions used to generate $T'_{1\rho}$ brain tissue image contrast provide a strategy to approach not only the intrinsic relaxation rate constants ($R_{1\rho A}$ and $R_{1\rho B}$) of two water populations, but also their fundamental properties (τ_c, r, P, and k). In the absence of CR, it is less likely that any populations detected reflect compartments.

An illustration of the sensitivity of the adiabatic $T_{1\rho}$ value to the molecular motional regime is illustrated in Fig. 4. Calculations were performed using the simple description of an isolated pair of identical spins (say, those of water) undergoing dipolar interaction; that is, combining Eqs. (6)–(8) (Table 1). The plots exhibit a greater general prolongation of $R_{1\rho,\,dd}$ during the HS4 pulse (Fig. 4b) as compared to the HS1 pulse (Fig. 4a). It can also be seen that the dependencies of $R_{1\rho,\,dd}$ on the AFP modulation functions (along the t-axis) is small for $\tau_c < 1$ ns. These plots can be thought of as simultaneously depicting the relaxation behaviors of two different populations (A and B) during adiabatic pulse modulation, if they have different τ_c values (say, τ_{cA} on the order of ns and τ_{cB} on the order of ps) and *if there is no exchange between them*. It can be seen that the $R_{1\rho,\,dd}(t)$ of site A (modeling macromolecule-interacting water) significantly depends on the pulse modulation functions, while the $R_{1\rho,\,dd}(t)$ of site B does not. The latter (site B) rapidly tumbling spins, with the small correlation time, can be thought to characterize relatively free tissue water molecules.

Fig. 4c makes it obvious that the shutter-speed $\tau_{1\rho}^{-1}(\equiv |R_{1\rho A} - R_{1\rho B}|)$ can vary greatly during the course of an AFP pulse. Its time-courses are plotted for two contiguous HS1 and two contiguous HS4 pulses (τ_{cA} and τ_{cB} were taken as 2.5 ns and 10 ps, respectively). It reaches a maximum of almost 45 s^{-1} at the mid-points of either the HS1 or HS4 pulse trains. This is probably more than an order of magnitude larger than its laboratory frame counterpart, $\tau_1^{-1}(\equiv |R_{1A} - R_{1B}|)$, for tissue water [33]. This means that $\tau_{1\rho}^{-1}$ has a much greater chance of moving an exchange system from the FXL (at the beginning and end of each pulse) into the intermediate exchange regime (which can be subdivided [17]). A horizontal dashed line for a k value of 15 s^{-1} is plotted in Fig. 4c. Since $\tau_{1\rho}^{-1}$ remains elevated for a much larger fraction of the HS4 pulse (and above k), the exchange should appear to slow to a greater extent using the HS4 pulse train than the HS1 train. Thus, it is gratifying that the brain HS4 data do indeed show a greater departure from monoexponentiality than the HS1 data (Fig. 2).

When exchange is admitted, then, theoretical simulations suggest that the small ($R'_{1\rho B}$), as well as the large ($R'_{1\rho A}$), *apparent* relaxation rate constant can also depend on the adiabatic pulse modulation functions used. Fig. 5 shows these dependencies on the HS1 and HS4 modulation functions, and on the water interproton vector correlation time in a slow tumbling site, A (τ_{cA}). The correlation time of the water interproton vector in a fast tumbling site, B, was taken as $\tau_{cB} = 76$ ps, and was kept constant. For these simulations, a model combining the dipolar relaxations between two identical spins with the 2SX (Eqs. (2), (3), (4), (6), (7), (8)) was used, with the parameters summarized in Table 1. We see that the $R'_{1\rho A}$ and the $R'_{1\rho B}$ values rise to be much larger than $R_{1\rho A}$ and $R_{1\rho B}$, respectively, because of the exchange kinetics (we used $k_A = 15\ s^{-1}$). Fig. 6 shows that the *apparent* populations (P'_A and P'_B) also depend on the adiabatic pulse modulation functions, as well as on the site A correlation time (τ_{cB} is still fixed). The values of P'_A and P'_B can be significantly different from the intrinsic populations used for these calculations: $P_A = 0.2$ and $P_B = 0.8$ (Table 1). The most important messages of Figs. 5 and 6 are that $R'_{1\rho A,B}$ and $P'_{A,B}$ vary *during* the adiabatic pulse (along the t-axis), and do so differently for the different adiabatic pulses. This means that Eq. (1) describes a multiexponential decay.

The isolated identical spin pair 2SX model has only six independent parameters. Thus, to further investigate exchange (issue 1), we have simulated the SI decay of the cortex tissue water measured with the $(HS1)_m$-90° and $(HS4)_m$-90° pulse sequences (lower red and black solid curves, respectively, in Fig. 2), using Eqs. (1), (2), (3), (4), (6), (7), (8), with the parameters listed in Table 1. The fundamental parameters are $\tau_{cA,B}$, $r_{A,B}$, $P_{A,B}$, and $k_{A,B}$. For the

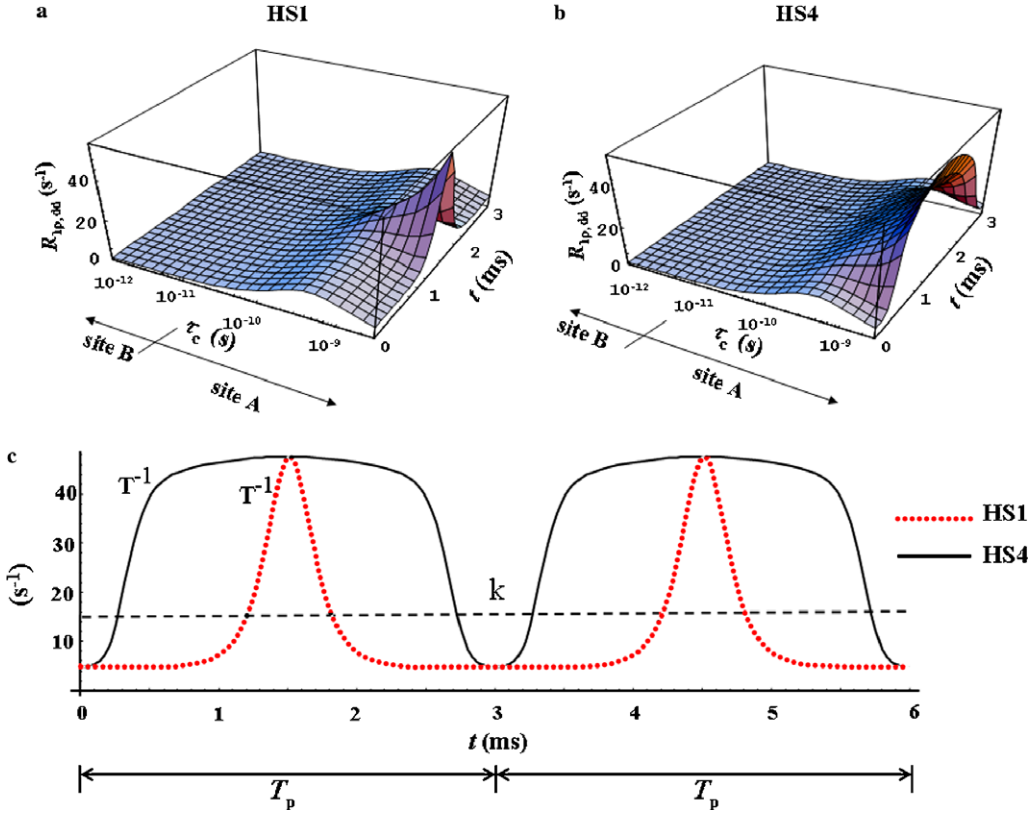

Fig. 4. The calculated variations of the intrinsic longitudinal rotating frame relaxation rate constant $R_{1\rho,\,dd}$ during the HS1 pulse (a) and HS4 pulse (b) are plotted as functions of the logarithm of the spin pair dipole rotational correlation time, τ_c. The equations and parameters used are listed in Table 1. Since the τ_c values range over three orders of magnitude, we can take those $>10^{-11}$ s to characterize site *A* (water interacting with a macromolecule) and those $<10^{-11}$ s to characterize site *B* (bulk-like water). The sites are *not* in equilibrium exchange. The equations and parameters used are listed in Table 1. (c) The time-courses of the shutter-speed, $\tau_{1\rho}^{-1}$, for two contiguous HS1 and two contiguous HS4 AFP pulses are shown (τ_{cA} and τ_{cB} were taken as 2.5×10^{-9} and 10^{-11} s, respectively). A horizontal dashed line also indicates the value (15 s^{-1}) of a rate constant maintained during an isothermal data acquisition.

Table 1
Simulation parameter values

Simulation	Equations used	τ_{cA} (ns)	τ_{cB} (ps)	r_A (Å)	r_B (Å)	k_A (s^{-1})	P_A
Fig. 2 (lyso.)	(1)–(4), (6)–(8)	0.021	2	1.58	1.58	3.3×10^{10}	0.16
Fig. 2 (cortex)	(1)–(4), (6)–(8)	5.6	76	1.58	1.58	15	0.2
Fig. 4	(6)–(8)	varied	varied	1.58	1.58	—	—
Figs. 5 and 6	(2)–(4), (6)–(8)	varied	76	1.58	1.58	15	0.2
Fig. 7a	(1)–(4), (6)–(8)	5.6	76	1.58	1.58	40	0.2
Fig. 7b	(1)–(4), (6)–(8)	5.6	76	1.58	1.58	5	0.2
Fig. 7c	(1)–(4), (6)–(8)	50	76	1.58	1.58	15	0.2
Fig. 7d	(1)–(4), (6)–(8)	5.6	76	1.58	1.58	15	0.1

$I = 1/2$; $\hbar = 1.05459\times10^{-27}$ erg s; $\gamma = 26.75\times10^{3}$ rad/(s G); $\omega_1^{max}/2\pi = 2.5$ kHz.

set ($\tau_{cA} = 5.6$ ns, $r_A = 1.58$ Å, $P_A = 0.2$, $k_A = 15\ s^{-1}$, $\tau_{cB} = 76$ ps, $r_B = 1.58$ Å, $P_B = 0.8$, and k_B ($= (P_A/P_B)k_A$) $= 3.75\ s^{-1}$ (Table 1)), the *simultaneous* agreement (solid curves) with the ten (or twelve) points of the lower HS1 and HS4 data sets (Fig. 2) is rather remarkable. We have not conducted a systematic search of the entire parameter space, and this result is not a formal fitting. However it is effectively such, since the positions and shapes of the TD-decay curve pairs turn out to be quite sensitive to parameter values. There are even parameter sets where the model HS4 decay curve (black) is above the model HS1 decay curve (red). These tend to be those in which both P_A (e.g., 0.05) and k_A (e.g., 0.1 s^{-1}) are smaller than the Table 1 values. Larger k_A values tend to linearize the curves (as we will see below). Thus, at this time, we can report that in order for this model to agree with all ten (or twelve) of the Fig. 2 brain data points, τ_{cA}, k_A, and P_A must be within ±4%, ±7%, and ±8% of the Table 1 values, respectively. The sensitivity of the theoretical curves to the model parameters is illustrated in Fig. 7. The parameter values used are also listed in Table 1. It can be seen that slight variations lead to a significant

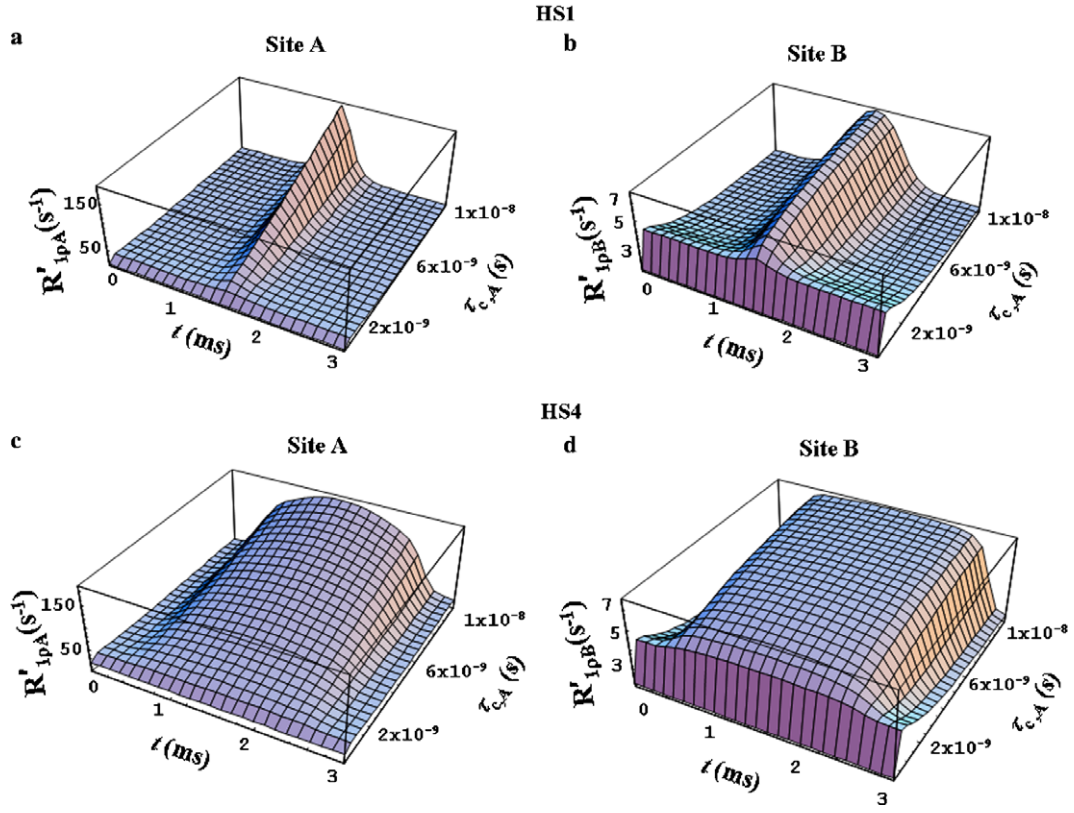

Fig. 5. The calculated variations of apparent longitudinal rotating frame relaxation rate constants $R'_{1\rho,A}$ (a and c) and $R'_{1\rho,B}$ (b and d), at two sites in equilibrium exchange, during the HS1 pulse (a and b) and the HS4 pulse (c and d) are plotted as functions of the rotational correlation time of a spin pair dipole in site A, τ_{cA}. The equations and parameters used are listed in Table 1.

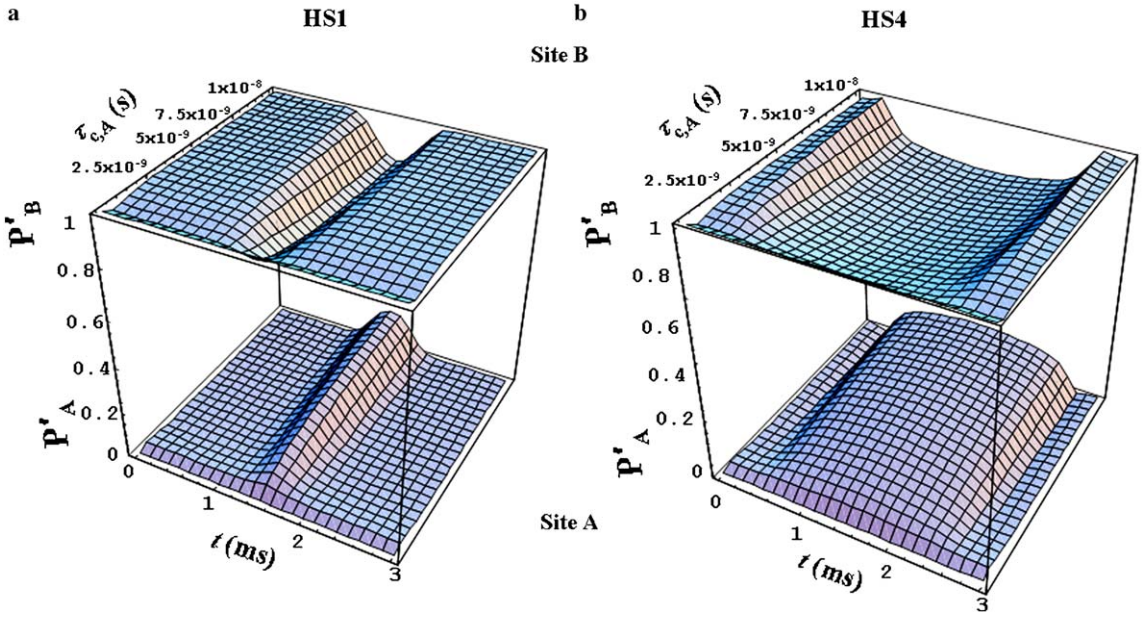

Fig. 6. The calculated variations of apparent populations P'_A and P'_B, at two sites in equilibrium exchange, during the HS1 pulse (a) and the HS4 pulse (b) are plotted as functions of the rotational correlation time constant for a spin pair dipole in site A, τ_{cA}. The equations and parameters used are listed in Table 1.

changes of the theoretical curves (panels a and b demonstrate the sensitivity to k_A; panel c to τ_{cA}; and panel d to P_A). The Fig. 2 cortex data points are re-plotted in each panel, in order to give a constant frame of reference. We did not systematically vary τ_{cB}, r_A, or r_B, though we found that we could not fix τ_{cB} to the 2 ps value for pure water.

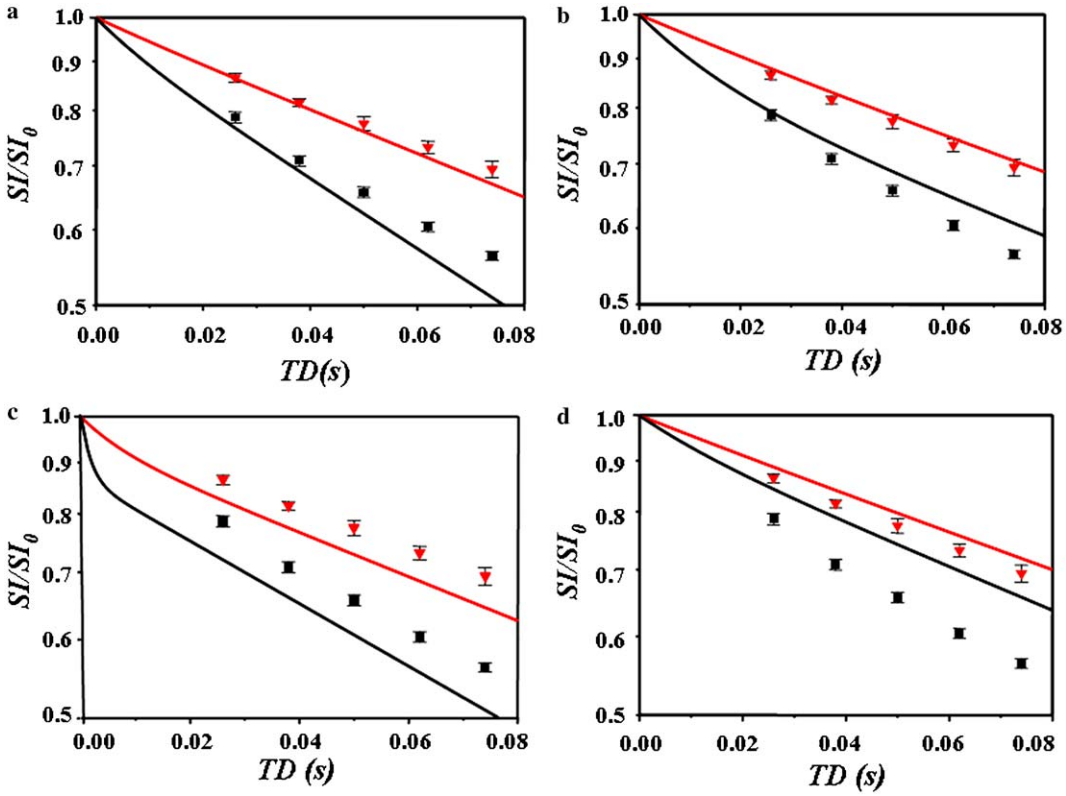

Fig. 7. As in Fig. 2, simulations of the logarithm of the normalized SI are plotted as functions of TD. These are separately calculated for the $(HS1)_m$-90° (red curves) and $(HS4)_m$-90° (black curves) pulse sequences, and use the equations and parameters listed in Table 1. The cortex points and error bars are the same as those in Fig. 2, and are repeated in each panel, for reference.

Thus, as far as sensitivity is concerned, the prospects for pixel-by-pixel fittings, and thus parametric mappings, are very encouraging. It is obvious from the empirical maps in Figs. 3b and c that there is considerable ROI-averaging in the Fig. 2 in vivo data. Analytical parametric maps could therefore be much more revealing. However, the noise in single pixel data is much greater, and we have not attempted fittings of these. But, we can make a rough approximation of a P_A map. If the monoexponential asymptotic decay of the data is taken to signify the FXL, then the observed rate constant is $P_A\langle R_{1\rho A}\rangle_t + P_B\langle R_{1\rho B}\rangle_t$, and is identified as $[R'_{1\rho B}]_{TD\to 0}$ (Eq. (5)) [17]. The fact that we have different asymptotic slopes for HS1 and HS4 acquisitions is supported by the model result that $R_{1\rho A}$ and $R_{1\rho B}$ have different dependencies on the two modulation functions (Fig. 4), and thus their time-averaged values, $\langle R_{1\rho A}\rangle_t$ and $\langle R_{1\rho B}\rangle_t$, differ. If we subtract the asymptotic HS1 rate constant from that of HS4, we can write:

$$[{}^{HS4}R'_{1\rho B}]_{TD\to 0} - [{}^{HS1}R'_{1\rho B}]_{TD\to 0} = [P_A\langle {}^{HS4}R_{1\rho A}\rangle_t + P_B\langle {}^{HS4}R_{1\rho B}\rangle_t] - [P_A\langle {}^{HS1}R_{1\rho A}\rangle_t + P_B\langle {}^{HS1}R_{1\rho B}\rangle_t] \quad (9)$$

Because the $\langle {}^{HS4}R_{1\rho B}\rangle_t$ and $\langle {}^{HS1}R_{1\rho B}\rangle_t$ values are very small (Fig. 4), and essentially equal, we can then write an approximate expression for the difference of asymptotic apparent $R_{1\rho}$ values of the two modulation functions, which is thus proportional to P_A.

$$[{}^{HS4}R'_{1\rho B}]_{TD\to 0} - [{}^{HS1}R'_{1\rho B}]_{TD\to 0} \approx P_A[\langle {}^{HS4}R_{1\rho A}\rangle_t - \langle {}^{HS1}R_{1\rho A}\rangle_t]. \quad (10)$$

In Fig. 8, asymptotic $T'_{1\rho}$ (8a,b), $R'_{1\rho}$ (8c,d), and difference $([{}^{HS4}R'_{1\rho B}]_{TD\to 0} - [{}^{HS1}R'_{1\rho B}]_{TD\to 0})$ (8e) maps from the axial slab of the Fig. 3 subject are shown. For this analysis an axial image slice was chosen because the coronal tangential slab contains large amounts of CSF. The difference map (Fig. 8e) clearly shows the greatest intensities in the cortex (where the P_A values are larger), and demonstrates good contrast with the adjacent subarachnoid CSF. The cortical/CSF interface is seen clearly in the T_1-weighted image of this plane (Fig. 8f). The asymptotic relaxation rate constants of the CSF, which has a large fraction of rapidly tumbling spins, are less affected by the adiabatic modulation than that of the brain tissue. This result further demonstrates the sensitivity of adiabatic $T_{1\rho}$ contrast to larger water correlation times ($\tau_c > 10^{-9}$ s), in agreement with the theoretical prediction. The noise is significant in the difference map (Fig. 8e) because it arises from subtractions of pairs of similarly sized numbers, and because the $(\langle {}^{HS4}R_{1\rho A}\rangle_t - \langle {}^{HS1}R_{1\rho A}\rangle_t)$ factor on the RHS of approximation (10) is not truly constant. In future work, it will be interesting to see if a true P_A map exhibits less noise.

The k_A and P_A values for the Fig. 2 brain curves are rather smaller and larger, respectively, than might conventionally be expected for the exchange of macromolecule-in-

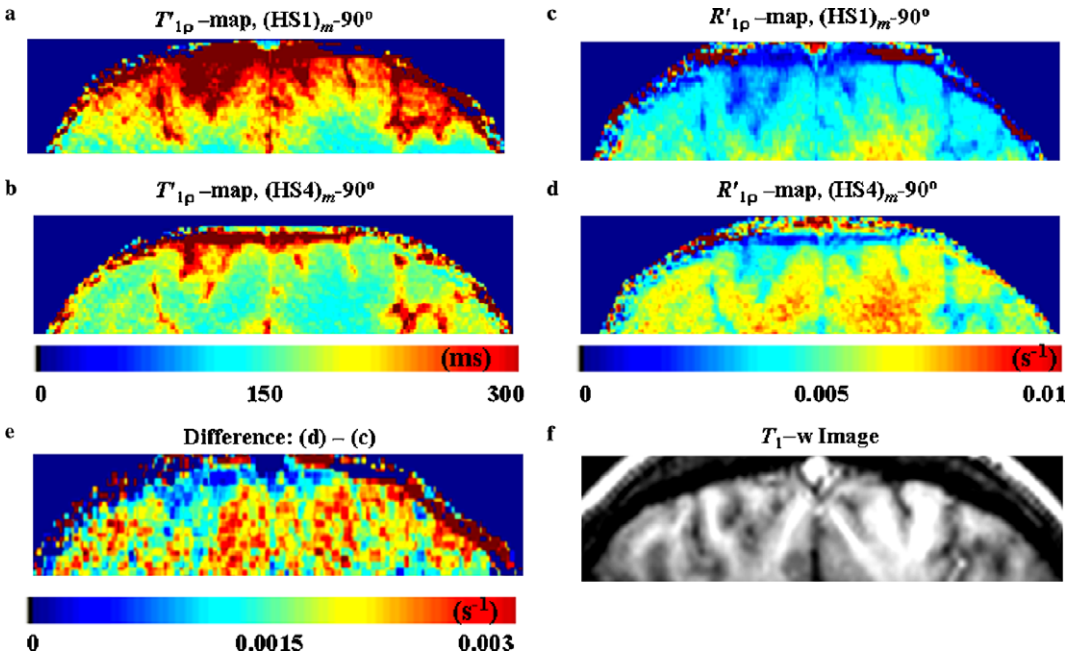

Fig. 8. The asymptotic $T'_{1\rho}$ -maps of an axial image slice, measured with the (a) $(HS1)_m$-90° and (b) $(HS4)_m$-90° pulse sequences, are displayed with the same color scale. The TurboFLASH imaging readout was used. The analogous asymptotic $R'_{1\rho}(\equiv 1/T'_{1\rho})$—maps obtained for the $(HS1)_m$-90° (c) and $(HS4)_m$-90° (d) pulse sequences are displayed with a constant color scale. (e) The asymptotic $R'_{1\rho}$ difference map, obtained by the subtraction (d) – (c), is shown. (f) The T_1-weighted axial image slice (containing the visual cortex V1) is shown for this subject (the same as in Fig. 3).

teracting water [A] with bulk-like water [B] [33,34]. The small exchange rate constant value of $k_A = 15\ s^{-1}$ in Table 1 might indicate that the mean residence time of the macromolecule-interacting water is heavily weighted by "internal" water, either (entropically) buried in cavities or trapped in narrow clefts, or by water (enthalpically) coordinated to diamagnetic metal ions [33,34]. The $R_{1\rho,\,dd}$ value is sensitive to molecular motions in the very low frequency regions of the spectral density. The AFP pulse modulation function effectively sweeps the system through υ_{eff} values (Eq. (6)) up to at most ~4 kHz (Fig. 1b). The root mean values of the ω_{eff} squares during the pulses (Fig. 1b) correspond to the proton Larmor frequencies at field values in the μT range. The large P_A value (0.2) might suggest that surface-interacting water molecules [33,34] are also included in population A. However, for actual tissue in vivo, there is surely a greater internal water fraction than in the relatively dilute solutions (often with unphysiological pH values) of relatively small macromolecules typically accessed by high-resolution NMR methods [33,34] (next paragraph). We note an interesting recent imaging report that at least 12% of excised rat brain ^1H_2O is sufficiently fluid to yield a relatively narrow spectral line despite being at a temperature where pure water is frozen and gives rise to a broad line [34]. Since this is rather uniformly distributed throughout the brain, it has been ascribed to macromolecule-interacting water [35]. We might eventually be able to depict such water in vivo, with P_A maps. It seems clear that the cavities for internal water molecules can be large enough to allow relatively small τ_{cA} values, such as the 5.6 ns of Table 1 [35], while at the same time also lowering k_A. Our results suggest that for reasonable simulation of the brain tissue ^1H_2O situation, the contribution of an isochronous 2SX should be included.

The results for the lysozyme solution (Fig. 2; Table 1)—a common model [36,37]—strongly support these interpretations. Lysozyme is a fairly small protein (14.3 kDa) with few buried water sites [34]. The concentration (20%) of the solution we studied is such that the macromolecular volume fraction is similar to that of the tissue studied [6b]. However, the $T'_{1\rho}$ decays are considerably slower, and each is clearly characterized as a single exponential ($^{HS1}R'_{1\rho} = 1.63\ s^{-1}$ (red); $^{HS4}R'_{1\rho} = 1.83\ s^{-1}$ (black)). The lines in Fig. 2 that are in good agreement with the data result from our model with $\tau_{cA} = 21$ ps, and $k_A = 3.3 \times 10^{10}\ s^{-1}$ (Table 1). These values are quite close to those expected for mostly surface-interacting water molecules [33,34]. In fact, the system is surely in the FXL, and significantly different k_A values would give the same straight lines. When a system is in the FXL, only a lower limit for the exchange rate constants can be determined [17], and analysis by the model is indeterminate. We have gone as low as $k_A = 10^5\ s^{-1}$ with no change. (Thus, the fact that the solution was at a lower temperature than the tissue is inconsequential.)

Further extension of the 2SX model to a three spin system in one site [27] could include the dipolar interaction order parameter [38], and could be combined with the experimental modification of different dipolar relaxation pathway weightings. Furthermore, assessment of an anisochronous exchange contribution (e.g., $\delta\omega \neq 0$) by varying the field strength, may be needed for the complete investi-

gation of the relaxation processes responsible for adiabatic $T'_{1\rho}$ contrast.

In addition, further developments (such as parallel imaging) can provide the possibility of practically obtaining whole-brain $T_{1\rho}$ maps using a multi-slice acquisition method. Because of SAR limitations, the number of AFP HS1 and HS4 pulses used in the current acquisition cannot be further increased. Thus, the sampling of data at longer TD values is prohibited.

7. Conclusion

In this work, we have shown how adiabatic pulses with different modulation functions can be exploited to directly assess $T_{1\rho}$ relaxation and to generate tissue contrast in human brain ^1H_2O images. One or more dipolar relaxation channels probably contribute to longitudinal relaxation during an AFP pulse train placed prior the excitation pulse. For the dipolar interaction between two identical spins, the dependence of the $T_{1\rho}$ time constant on the AFP pulse modulation functions is insignificant for $\tau_c < 1$ ns. It was shown that the *adiabatic* $R'_{1\rho}$ contrast differences obtained using different modulation functions (HS1 and HS4) can be quite well described by a two-site-exchange model. This can provide intrinsic relaxation parameters of the specific site A (or B) undergoing equilibrium exchange. In the presence of the 2SX, the apparent relaxation rate constants and populations of the two sites depend on the modulation functions used. We find that the pertinent shutter-speed, $\tau^{-1}_{1\rho}(\equiv| R_{1\rho A} - R_{1\rho B} |)$, can vary greatly during the course of an AFP pulse train, and differently for different modulation functions, while of course the actual exchange kinetics are invariant. This means that the exchange condition varies significantly during the pulse, and this provides the opportunity to assess low frequency motional regimes in living tissue.

A model of dipolar relaxations between two identical spins was used for a description of the $T_{1\rho}$ contrast generated in the human brain images. A combination of full relaxation matrices (i.e., dipolar auto-relaxations, cross-relaxations and cross-correlations) with an isochronous equilibrium exchange may be necessary for a complete description of adiabatic $T_{1\rho}$ contrast in tissue. Because adiabatic ^1H_2O $T_{1\rho}$ contrast probably originates predominantly from dipolar relaxation pathways, while adiabatic $T_{2\rho}$ contrast may originate from the averaging of other interactions, these two measurements may prove complementary. We believe that adiabatic $T_{2\rho}$ and $T_{1\rho}$ contrast methods can be unique for the characterization of various diseases, and hold great potential for investigation and diagnosis of neurodegenerative disorders, cancer and stroke.

Acknowledgments

This work was partially supported by NIH Grants CA92004, RR08079, NS40801, and EB00422, the Keck Foundation, and the MIND Institute. We thank Drs. Xin Li, William Rooney, and Amy Springer for stimulating discussions.

References

[1] O. Gröhn, H. Mäkelä, J. Lukkarinen, L. DelaBarre, J. Lin, M. Garwood, R. Kauppinen, On- and off-resonance $T_{1\rho}$ MRI in acute cerebral ischemia of the rat, Magn. Reson. Med. 49 (1) (2003) 172–176.

[2] S. Akella, R. Regatte, A. Wheaton, A. Borthakur, R. Reddy, Reduction of residual dipolar interaction in cartilage by spin-lock technique, Magn. Reson. Med. 52 (5) (2004) 1103–1109.

[3] A. Wheaton, A. Borthakur, M. Cordo, G. Moonis, E. Melhem, R. Reddy, $T_{2\rho}$-weighted contrast in MR images of the human brain, Magn. Reson. Med. 52 (6) (2004) 1223–1227.

[4] S. Michaeli, H. Gröhn, O. Gröhn, D. Sorce, R. Kauppinen, C. Springer, K. Ugurbil, M. Garwood, Exchange-Influenced $T_{2\rho}$ contrast in human brain images measured with adiabatic radio frequency pulses, Magn. Reson. Med. 53 (2005) 823–829.

[5] S. Taheri, R. Sood, Spin-lock MRI with amplitude- and phase-modulated adiabatic waveforms: an MR simulation study, Magn. Reson. Imaging 24 (2006) 51–59.

[6] (a) E. Andrew, G. Bydder, J. Griffiths, R. Iles, P. Styles, Clinical Magnetic Resonance: Imaging and Spectroscopy, Wiley, Chichester, 1980, p. 36;
(b) W. Rooney, G. Johnson, X. Li, E. Cohen, S.-G. Kim, K. Ugurbil, C. Springer, The magnetic field and tissue dependence of human brain longitudinal ^1H_2O relaxation in vivo, Magn. Reson. Med., under revision.

[7] S. Tanny, M. Pickering, C. Springer, Increasing the time resolution of dynamic nuclear magnetic resonance spectroscopy through the use of lanthanide shift reagents, J. Am. Chem. Soc. 95 (1973) 6227–6232.

[8] R. Sepponen, J. Pohjonen, J. Sipponen, J. Tanttu, A method for $T_{1\rho}$ imaging, J. Comput. Assist. Tomog. 9 (1995) 1007–1011.

[9] G. Santyr, E. Fairbanks, R. Kelcz, J. Sorensen, Off-resonance spin locking for MR imaging, Magn. Reson. Med. 32 (1994) 43–51.

[10] M. Garwood, L. DelaBarre, The return of the frequency sweep: designing adiabatic pulses for contemporary NMR, J. Magn. Reson. 153 (2001) 155–177.

[11] S. Michaeli, D. Sorce, D. Idiyatullin, K. Ugurbil, M. Garwood, Transverse relaxation in the rotating frame induced by chemical exchange, J. Magn. Reson. 169 (2004) 293–299.

[12] D. Woessner, Nuclear transfer effects in nuclear magnetic resonance pulse experiments, J. Chem. Phys. 35 (1) (1961) 41–48.

[13] D. Woessner, J. Zimmerman, Nuclear transfer and anisotropic motional spin phenomena: relaxation time temperature dependence studies of water adsorbed on silica gel. IV, J. Phys. Chem. 67 (1963) 1590–1600.

[14] D. Davis, M. Perlman, R. London, Direct measurements of the dissociation-rate constant for inhibitor-enzyme complexes via the $T_{1\rho}$ and T_2 (CPMG) methods, J. Magn. Reson. B 104 (1994) 266–275.

[15] A. Palmer, C. Kroenke, J. Loria, Nuclear magnetic resonance methods for quantifying microsecond-to-millisecond motions in biological macromolecules, Methods Enzymol. 339 (2001) 204–238.

[16] M. Fischer, A. Majumdar, E. Zuiderweg, Protein NMR relaxation: theory, applications and outlook, Progr. NMR Spectrosc. 33 (1998) 207–272.

[17] J. Lee, C. Springer, Effect of equilibrium exchange of diffusion - weighted NMR signals: the diffusigraphic "Shutter-speed", Magn. Reson. Med. 49 (2003) 450–458.

[18] H. McConnell, Reaction rates by nuclear magnetic resonance, J. Chem. Phys. 28 (1958) 430–431.

[19] J. Blicharski, Nuclear magnetic relaxation in rotating frame, Acta Phys. Pol. A 41 (2) (1972) 223–236.

[20] A. Tannus, M. Garwood, Improved performance of frequency-swept pulses using offset-independent adiabaticity, J. Magn. Reson. A 120 (1996) 133–137.

[21] M. Silver, R. Joseph, D. Hoult, Highly selective π/2 and π pulse generation, J. Magn. Reson. 59 (1984) 347–351.
[22] R. Gruetter, I. Tkac, Field mapping using reference scan using asymmetric eco-planar technique, Magn. Reson. Med. 43 (2000) 319–323.
[23] A. Haase, Snapshot FLASH MRI: application to T_1-, T_2-, and chemical shift imaging, Magn. Reson. Med. 13 (1990) 77–89.
[24] I. Tkac, Z. Starcuk, I. Choi, R. Gruetter, In vivo ^{1}H NMR spectroscopy of rat brain at 1 ms echo time, Magn. Reson. Med. 41 (1999) 649–656.
[25] J. Pfeuffer, P. Moortele, K. Ugurbil, X. Hu, G. Glover, Correction of physiologically induced global off-resonance effects in dynamic echo-planar and spiral functional imaging, Magn. Reson. Med. 47 (2002) 344–353.
[26] M. Levitt, R. Freeman, T. Frenkel, Broadband heteronuclear decoupling, J. Magn. Reson. 47 (1982) 328–330.
[27] I. Burghardt, R. Konrat, G. Bodenhausen, Measurement of cross-correlation of fluctuations of dipolar couplings and anisotropic chemical shifts by selective spin locking, Mol. Phys. 75 (2) (1992) 467–486.
[28] J. Quirk, G. Bretthorst, T. Duong, A. Snyder, C. Springer, J. Ackerman, J. Neil, Equilibrium water exchange between the intra-and extracellular spaces of mammalian brain, Magn. Reson. Med. 50 (3) (2003) 493–499.
[29] T. Yankeelov, W. Rooney, W. Huang, J. Dyke, X. Li, A. Tudorika, J. Lee, J. Koutcher, C. Springer, Evidence for shutter-speed variation in CR bolus-tracking studies of human pathology, NMR Biomed. 18 (2005) 173–185.
[30] T. Yankeelov, W. Rooney, X. Li, C. Springer, Variation of the relaxographic "shutter-speed" for transcytolemmal water exchange affects the CR bolus-tracking curve shape, Magn. Reson. Med. 50 (6) (2003) 1151–1169.
[31] X. Li, W. Huang, T. Yankeelov, A. Tudorica, W. Rooney, C. Springer, Shutter-speed analysis of contrast reagent bolus-tracking data: preliminary observations in benign and malignant breast disease, Magn. Reson. Med. 53 (3) (2005) 724–729.
[32] R. Zhou, S. Pickup, T. Yankeelov, C. Springer, J. Glickson, Simultaneous measurement of arterial input function and tumor pharmacokinetics in mice by dynamic contrast enhanced imaging: effects of transcytolemmal water exchange, Magn. Reson. Med. 52 (2) (2004) 248–257.
[33] K. Venu, V. Denisov, B. Halle, Water ^{1}H magnetic relaxation dispersion in protein solutions. A quantitative assessment of internal hydration, proton exchange, and cross-relaxation, J. Am. Chem. Soc. 119 (1997) 3122–3134.
[34] V. Denisov, B. Halle, Protein hydration dynamics in aqueous solution, Faraday Discuss. 193 (1996) 227–244.
[35] A. Oros, J. Kaffanke, N. Shaw, Imaging of bound water in the frozen rat brain, in: Proc. Int. Soc. Magn. Reson. Med. (2005) pp. 2480.
[36] J. Korb, R. Bryant, Magnetic field dependence of proton spin-lattice relaxation times, Magn. Reson. Med. 48 (2002) 21–26.
[37] C. Lester, R. Bryant, Water-proton nuclear magnetic relaxation in heterogeneous systems: hydrated lysozyme results, Magn. Reson. Med. 22 (1991) 143–153.
[38] L. Vugmeyster, P. Pelupessy, B. Vugmeister, D. Abergel, G. Bodenhausen, Cross-correlated relaxation in NMR of macromolecules in the presence of fast and slow internal dynamics, C. R. Physique 5 (2004) 377–386.